The Astrophysical Journal Letters, 709:L88–L93, 2010 January 20 doi:10.1088/2041-8205/709/1/L88

THE NASCENT FAST SOLAR WIND OBSERVED BY THE EUV IMAGING SPECTROMETER ON BOARD HINODE

Hui Tian[1], Chuanyi Tu[1], Eckart Marsch[2], Jiansen He[2], and Suguru Kamio[2]
[1] School of Earth and Space Sciences, Peking University, 100871 Beijing, China; tianhui924@gmail.com
[2] Max-Planck-Institut für Sonnensystemforschung, 37191 Katlenburg-Lindau, Germany
Received 2009 October 24; accepted 2009 December 21; published 2010 January 5

ABSTRACT

The origin of the solar wind is one of the most important unresolved problems in space and solar physics. We report here the first spectroscopic signatures of the nascent fast solar wind on the basis of observations made by the EUV Imaging Spectrometer on Hinode in a polar coronal hole in which patches of blueshift are clearly present on Dopplergrams of coronal emission lines with a formation temperature of $\lg(T/\mathrm{K}) > 5.8$. The corresponding upflow is associated with open field lines in the coronal hole and seems to start in the solar transition region and becomes more prominent with increasing temperature. This temperature-dependent plasma outflow is interpreted as evidence of the nascent fast solar wind in the polar coronal hole. The patches with significant upflows are still isolated in the upper transition region but merge in the corona, in agreement with the scenario of solar wind outflow being guided by expanding magnetic funnels.

Key words: solar wind – Sun: corona – Sun: transition region – Sun: UV radiation

Online-only material: color figures

1. INTRODUCTION

As one of the most important unresolved problems in space and solar physics, the origin of the solar wind has received much attention and has been studied intensively since the solar wind was discovered. While it is well established that coronal holes are the source regions of the fast solar wind (e.g., Krieger et al. 1973; Bell & Noci 1976; McComas et al. 1998; Kohl et al. 2006), the sources of the slow solar wind remained unclear. Several possible solar locations have been suggested, including boundaries of polar coronal holes and helmet streamers (e.g., Gosling et al. 1981; Wang et al. 1990; Antonucci 2006; Noci & Gavryuseva 2007), small open-field regions embedded in the quiet Sun (He et al. 2007; Tian et al. 2008b; He et al. 2009; Tian et al. 2009), and edges of active regions (Kojima et al. 1999; Sakao et al. 2007; Marsch et al. 2008).

Possible spectroscopic signatures of the nascent fast solar wind have been intensively studied and identified in the past decade, in particular on the basis of observations made by the Solar Ultraviolet Measurements of Emitted Radiation (SUMER, Wilhelm et al. 1995; Lemaire et al. 1997) instrument on *SOHO*. Particularly, the Ne VIII (λ770) line, formed in the upper transition region (TR) at approximately $\lg(T/\mathrm{K}) = 5.8$, was found to be blueshifted on average in coronal holes (Dammasch et al. 1999; Peter & Judge 1999; Wilhelm et al. 2000; Xia et al. 2003; Aiouaz et al. 2005; McIntosh et al. 2007; Tian et al. 2008a, 2008c). Two-dimensional images of the Doppler shift of Ne VIII revealed blueshifts of 3–6 km s^{-1} along the network lanes in polar coronal holes (Hassler et al. 1999; Wilhelm et al. 2000). These patches of blueshift were found to be associated with coronal magnetic funnels and were interpreted as the initial outflow of the fast solar wind (Tu et al. 2005).

Due to the lack of strong coronal emission lines in the SUMER spectra, two-dimensional Dopplergrams of emission lines with a formation temperature higher than that of Ne VIII could not be derived in coronal holes. Yet recent observations with the EUV Imaging Spectrometer (EIS, Culhane et al. 2007) on board Hinode revealed clear blueshifts at the edges of active regions. The speed of this upflow increases with increasing temperature, from about 3 km s^{-1} at $\lg(T/\mathrm{K}) = 5.8$ to 28 km s^{-1} at $\lg(T/\mathrm{K}) = 6.3$ (Del Zanna 2008). This steady plasma outflow was interpreted as an indicator of the nascent slow solar wind (Harra et al. 2008). A similar study of the velocity structures in coronal holes, however, is hampered significantly by the weakness of the emission there, and thus spectroscopic signatures of the nascent fast solar wind in coronal holes have not yet been identified by using EIS data.

In this Letter, we will present such results derived from a data set obtained by EIS with a very long exposure time of 150 s, and thus we can report here the first identification of spectroscopic signatures of the nascent fast solar wind from EIS observations in a polar coronal hole.

2. DATA REDUCTION AND ANALYSIS

The EIS data analyzed here were acquired at the northern polar region from 14:13 to 18:17 UT on 2007 October 10. This data set was previously analyzed by Banerjee et al. (2009) to search for signatures of Alfvén waves. The combination of using the 2″ slit and a very long exposure time of 150 s greatly improved the count statistics, and thus allows for a reliable derivation of the Doppler shifts from the line profiles. The raster increment was about 2″, and 101 exposures were made during the scan, so that the scanned region has a size of about 200″ × 512″. The wavelengths and formation temperatures of the selected lines are listed in Table 1.

The standard EIS correction routine *eis_prep.pro* available in the SolarSoft (SSW) package was adopted to calibrate the data, including subtraction of the dark current, removal of cosmic rays and hot pixels, and radiometric calibration. The amount of slit tilt has been estimated by averaging the velocities along each row from a large raster of the quiet Sun taken early in the mission (Mariska et al. 2007). It was removed by applying the SSW routine *eis_slit_tilt.pro*. To correct for the orbital variation caused by thermal effects on the instrument, we first summed up all profiles of the strong line Fe XII 195.12 in each exposure,

Table 1
Emission Lines Used for this Study

Ion	λ (Å)	lg(T/K)	Ion	λ (Å)	lg(T/K)
He II	256.32	4.70	Fe X	184.54	6.00
O V	192.90	5.40	Fe XII	195.12	6.11
Mg VI	270.39	5.60	Fe XIII	202.04	6.20
Fe VIII	185.21	5.60	Fe XIV	270.52	6.25
Si VII	275.35	5.80	Fe XV	284.16	6.30

Note. Here λ represents the wavelength and T the formation temperature of the emission line.

and then calculated the spectral position of the line center for each summed profile. The resulting temporal evolution of the line center position was used to eliminate the orbital variation in all lines. The corrections of the slit tilt and orbital variation were applied to the wavelength vector at each spatial location of an image before further data processing.

By calculating the cross correlation between the intensity images of the lines He II 256.32 and O V 192.90, we found an offset by 17″ in the north–south direction between the images in these two EIS wavelength bands. We therefore chose the common regions where the observations in different lines overlap, and subsequently reduced the size of the studied region to 200″ × 478″. Then we averaged the resulting data over two pixels along the slit to improve the signal-to-noise ratio and made the pixel size comparable in both dimensions of solar-X and solar-Y. Finally, a running average over 3 pixels in both spatial dimensions was applied to the data, which again greatly improved the signal-to-noise ratio.

A single Gaussian fit was then applied to each line profile that is clean from blends. According to Young et al. (2007), the Fe VIII 185.21, Si VII 275.35, Fe X 184.54, Fe XII 195.12, and Fe XIII 202.04 line profiles in our data can all be approximated well by a single Gaussian. The Fe VIII 185.21 line is blended with the Ni XVI 185.23 line in active regions, but in the quiet Sun and coronal holes this blend is almost absent. The Mg VI 270.39 and Fe XIV 270.52 lines are blended with each other, and therefore we used a double-Gaussian-fitting procedure to separate them. The Fe XV 284.16 line is weakly blended with Al IX 284.03, and a double-Gaussian fit was applied for their decomposition. There are several lines (namely O V 192.80, Fe XI 192.83, Ca XVII 192.82) on the blue wing of O V 192.90, and thus we also had to use a double-Gaussian fit to extract the line profile of O V 192.90, thereby treating the three blends as one Gaussian component, respectively. The He II 256.32 line and its blends are difficult to separate, and thus we did not use this line for our spectroscopic study. The line radiance and central position of every profile were thus obtained from the fits. However, although we have improved the signal-to-noise ratio a lot, there are still many profiles which cannot be well fitted, especially those of weak lines. Thus, in Figure 1, we only present maps of radiance and Doppler shift for four strong lines and exclude the northern most part of the field of view (FOV).

We further selected several subregions from the FOV, which are outlined by dashed rectangles in Figure 1. Regions 1 and 5 correspond to the quiet Sun and coronal hole, respectively. Regions 2–4 are small sub-regions where significant blueshift of Fe XIII is present inside the coronal hole. For each line, the profiles in each region were averaged. These profiles are all good enough to permit reliable Gaussian fits. Several examples of the averaged line profiles are presented in Figure 2.

The rest wavelengths were determined by assuming a zero shift of the accumulated emission at positions between 65″ and 143″ above the limb (the northern most part of the FOV). Here the limb refers to the radial position where the radiance of Si VII 275.35 maximizes. This assumption is reasonable because non-radial velocities usually cancel in the corona (Kamio et al. 2007), and dynamic events are very rare in such high altitudes. In this way, we determined the rest wavelength of each line, and thus obtained the absolute Doppler shift. The emission of the Mg VI 270.39 and O V 192.90 lines was very weak between 65″ and 143″ above the limb, and consequently the fitting errors were very large. From Chianti (Dere et al. 1997; Landi et al. 2006), we know the spectral distance between Mg VI 270.39 and Fe XIV 270.52. So the rest wavelength of Mg VI 270.39 could be calculated by subtracting this spectral distance from the rest wavelength of the Fe XIV 270.52 line. But we could not use this method for the O V 192.90 line, since its blends were too complicated. Instead, we simply assumed a net redshift of 6 km s^{-1} in the quiet Sun (region 1), following the statistical result in Figure 8 of Xia et al. (2004).

The absolute Doppler shift of each line in different selected regions is presented in Figure 3. Here positive and negative values correspond to redshift and blueshift, respectively. In Figure 3(d), we present the temperature dependence of the difference between Doppler shift for the averaged profiles in the coronal hole (region 5) and quiet Sun (region 1). The Doppler shifts in regions 1–5 have been divided by 0.71, 0.37, 0.44, 0.43, and 0.37, respectively, to account for the line-of-sight effect under the assumption of radial outflows.

3. RESULTS AND DISCUSSION

In the past ten years, SUMER observations have contributed a lot to our understanding of the origin of the fast solar wind. Dopplergrams of the upper-TR line Ne VIII (λ770) revealed prevailing blueshifts in coronal holes, which was interpreted as a signature of the nascent fast solar wind. However, because of the lack of strong hotter lines in the SUMER spectra, higher temperature (e.g., lg(T/K) > 5.8) spectroscopic information on the initial outflow of the fast solar wind was still missing.

By analyzing the spectra acquired by EIS, we have managed to produce new two-dimensional images of the Doppler shift in a coronal hole for several emission lines with formation temperatures higher than that of Ne VIII. Patches of significant blueshift are clearly present in the coronal hole on the Dopplergrams of coronal emission lines with a formation temperature higher than lg(T/K) = 6.0. At some locations, the blueshift can reach ∼20 km s^{-1}. While outside the coronal hole there is mainly redshift and weak blueshift, as can be seen in Figure 1. In Figure 4, we illustrate magnetic field lines which were obtained by using the potential field source surface (PFSS) model (Schrijver 2001). It is very clear that the significant blueshifts in the coronal hole are associated with open field lines, and thus should be an indicator of the solar wind outflow.

Several coronal bright points (BPs) are also present in the coronal hole studies here. However, all of these bright points reveal blueshifts on one side and redshifts on the other side, which we interpret as spectroscopic signatures of siphon flows along the loops associated with the BPs. These adjacent downflows and upflows might also be signatures of the outward flows that are produced by magnetic reconnection in BPs (Brosius et al. 2007; Tian et al. 2008d).

The outflow in the coronal hole seems to start in the TR. The Dopplergram of the Si VII line reveals some patches of weak blueshift in the coronal hole. There are more blueshift patches

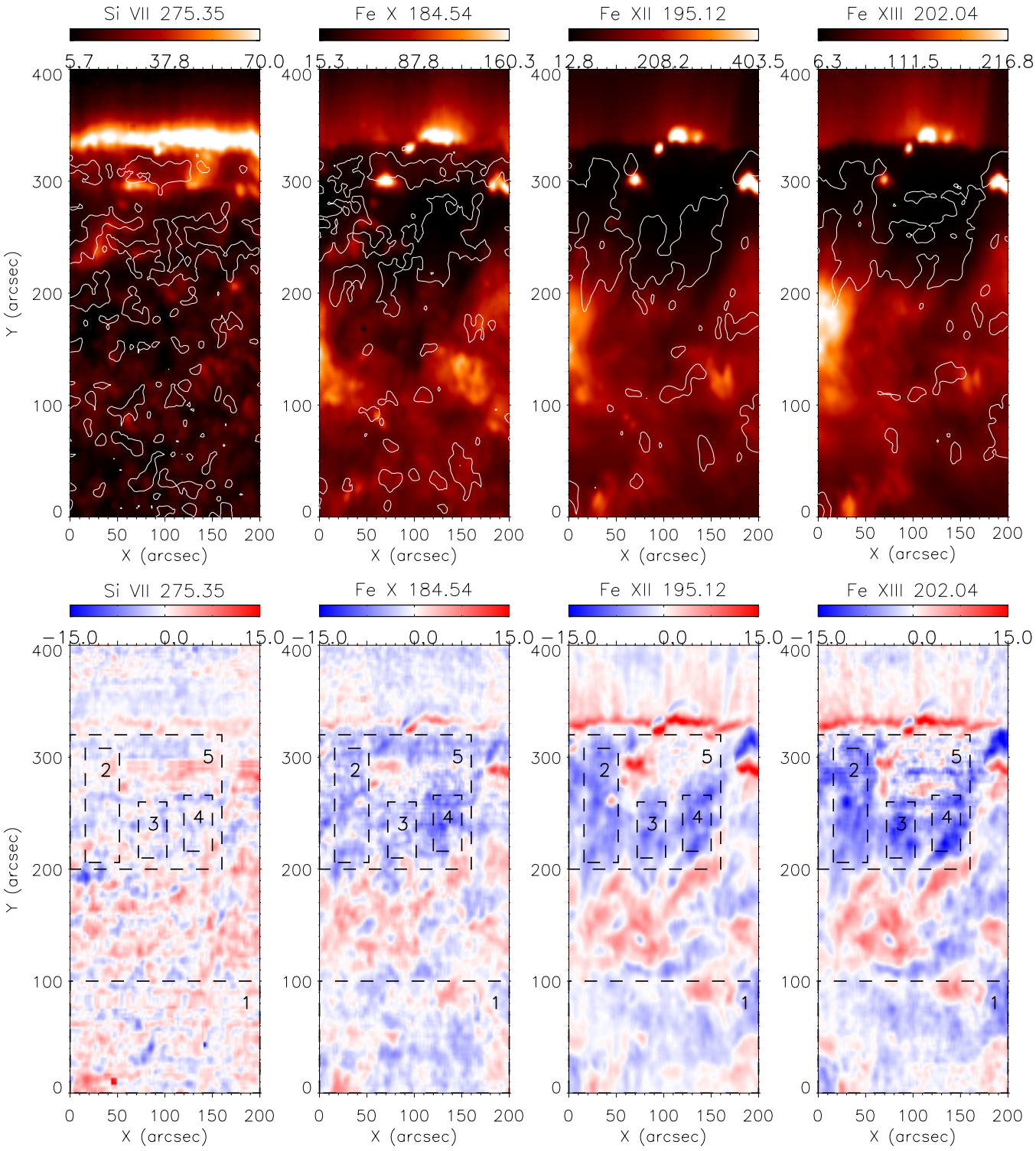

Figure 1. Maps of radiance (upper panels) in arbitrary units and Doppler shift (lower panels) in color-coded units of km s^{-1} for four emission lines. Contours enclosing the lowest 20% of the Doppler values are overplotted on the radiance map of the corresponding line. The dashed lines on the Dopplergrams outline the rectangular regions in which the profiles of each line as listed in Table 1 were accumulated and further studied.

(A color version of this figure is available in the online journal.)

inside the coronal hole than outside. We notice that the formation temperature of Si VII is similar to Ne VIII. However, the blueshift of Si VII in this coronal hole seems to be less prominent than that of Ne VIII in the polar coronal holes observed by SUMER. There are several possible explanations for this non-consistency. First, the rest wavelength determined by us might not be accurate. The TR is known to be much more dynamic than the corona, and thus the TR emission is more likely influenced by such plasma dynamics as related to spicules. As a result, the average TR line in the off-limb region might deviate from its rest wavelength. Second, most of the Ne VIII-related coronal hole studies were based on observations made in the last solar minimum, during which coronal holes might have had properties different from those in the current peculiar solar minimum.

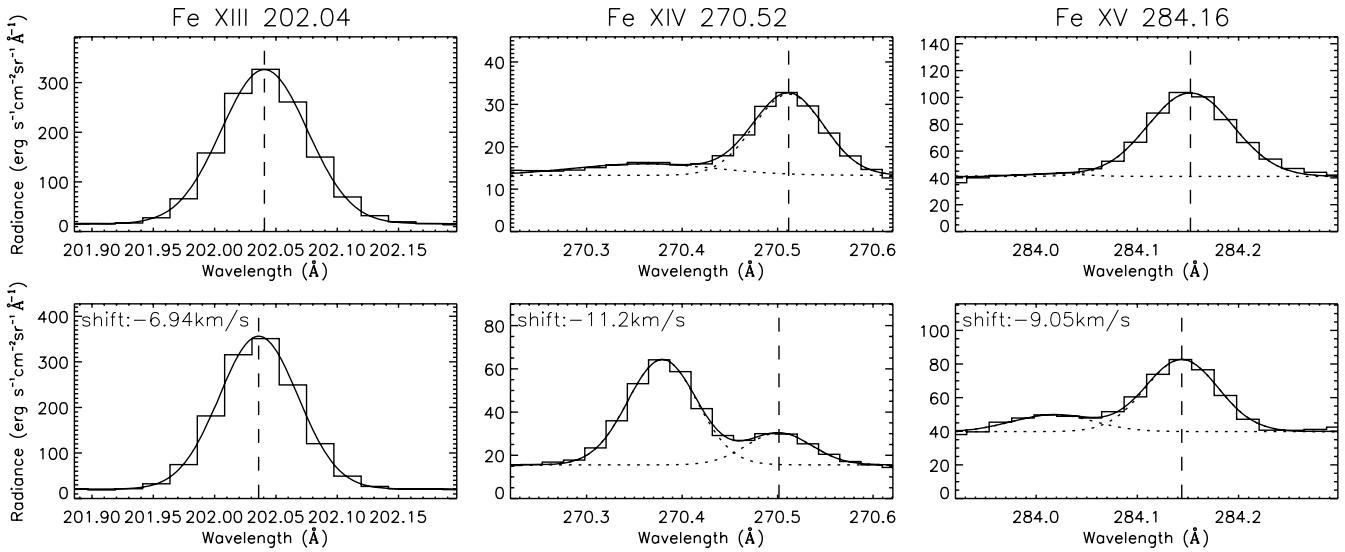

Figure 2. Averaged line profiles at positions between 65″ and 143″ above the limb (upper) and region 3 (lower) for three emission lines. The observed and fitted line profiles are represented by the histograms and solid curves, respectively. For the blended lines, the two Gaussian components are shown as two dotted curves. The vertical dashed lines indicate the central spectral positions. The absolute Doppler shift as revealed from the averaged profile in region 3 is also shown for each line.

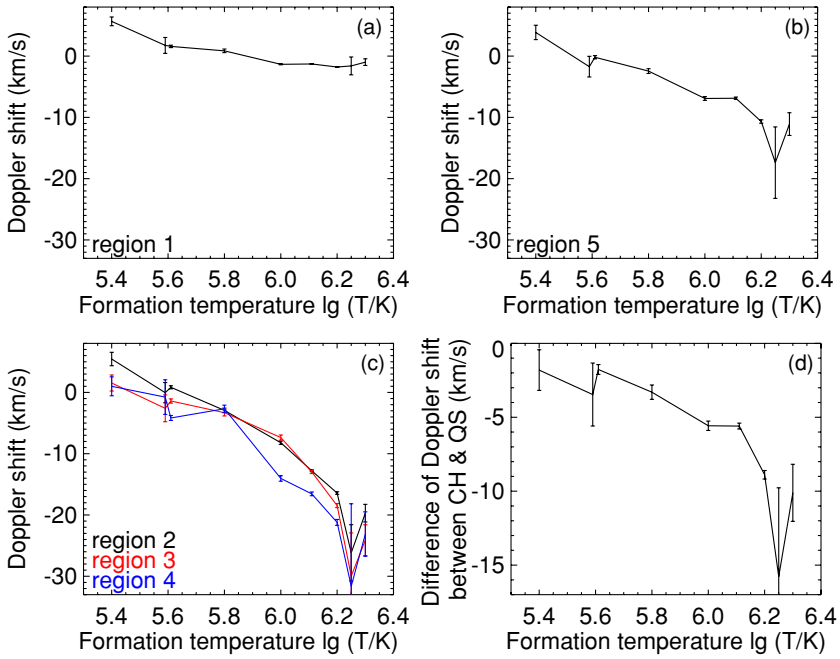

Figure 3. (a)–(c) Temperature dependence of the Doppler shift for various profiles averaged over several selected regions. The error bars represent the corresponding fitting errors of the line centers. (d) Temperature dependence of the difference between the Doppler shifts for the averaged profiles in the coronal hole (region 5) and quiet Sun (region 1). The error bars represent the uncertainties originating from the corresponding fitting errors of the line centers. To avoid overlapping, the data points for the Mg VI and Fe VIII lines are plotted at $\lg(T/\mathrm{K}) = 5.59$ and $\lg(T/\mathrm{K}) = 5.61$, respectively.

(A color version of this figure is available in the online journal.)

The pattern of the contours enclosing the lowest 20% of the Doppler values presented in Figure 1 reveals a clear dependence on the temperature. In the coronal hole, these contours are isolated when seen in the upper-TR line Si VII. The contours seem to expand with increasing temperature and finally merge in the corona at around $\lg(T/\mathrm{K}) = 6.2$. This behavior agrees with the scenario of solar wind outflow being guided by the expanding magnetic funnels (Tu et al. 2005), if we assume that lines with a higher formation temperature are formed in higher atmospheric layers. Several small funnels which originate from different parts of the chromospheric network expand with height and finally merge into a single open field region (Tian et al. 2008b). The nascent solar wind is guided through these funnel structures.

The temperature variation of the Doppler shift for the averaged profiles in the quiet Sun (region 2) shows a trend similar to the SUMER results at $\lg(T/\mathrm{K}) \leqslant 6.0$ (Peter & Judge 1999; Xia et al. 2004), from redshift in the middle-TR to blueshift in the upper-TR. Figure 3 reveals that above $\lg(T/\mathrm{K}) = 6.0$ the averaged profiles in the quiet Sun have very small blueshifts ($\sim$1.5 km s^{-1}), which seem to be independent of the temperature. This result confirms that our determination of the rest wavelengths is reasonable, since the quiet-Sun emission at coronal temperatures usually is assumed to be at rest on average (e.g., Milligan & Dennis 2009).

In the coronal hole, the O V line also has a net redshift. However, from Figure 3, we can see that the value of the

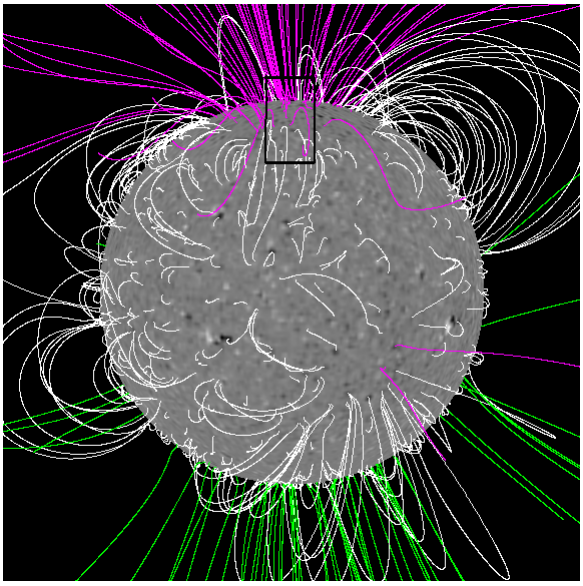

Figure 4. Magnetic field structure of the Sun at 18:06 on 2007 October 10, obtained by using the PFSS package available in SSW. Open field lines with different polarities passing through the source surface at 2.5 solar radii are illustrated in red and green, respectively. Closed field lines are shown in white. The rectangle outlines the observation region of EIS.

(A color version of this figure is available in the online journal.)

redshift is smaller in the coronal hole than in the quiet Sun. The transition from the redshift to the blueshift seems to occur at around $\lg(T/\mathrm{K}) = 5.6$, above which a clear increasing trend of the blueshift with increasing temperature can be seen in each selected region of the coronal hole. This blueshift reaches 25 km s^{-1} at around $\lg(T/\mathrm{K}) = 6.3$, after having taken the line-of-sight effect into account. Since emission lines with higher formation temperatures are usually formed in higher layers, the temperature-dependent blueshift revealed in Figure 3 is likely to be a signature of the initial acceleration of the fast solar wind.

Based on observations of the Ultraviolet Coronagraph Spectrometer (UVCS, Kohl et al. 1995), the speed of the nascent fast solar wind along field lines in the extended corona has been measured by using the Doppler dimming technique (e.g., Giordano et al. 2000; Teriaca et al. 2003; Gabriel et al. 2003; Kohl et al. 2006; Antonucci 2006; Telloni et al. 2007). However, in the inner corona, the radial evolution of the outflow speed has not been well determined. SUMER measurements at off-limb positions can only provide the line-of-sight component of the velocity, which is usually very small and largely different from the real radial outflow speed. SUMER can measure a large fraction of the real radial outflow speed at disk positions, but the information on the velocity in the corona is missing due to the lack of coronal lines in the SUMER spectral range. Our results based on EIS observations reveal important information on this missing part, and thus provides further observational constraints on future solar wind models.

When looking at Figure 1, the significant redshifts of the Fe XII and Fe XIII lines at the limb appear puzzling to us, if we assume that non-radial velocities are cancelling each other at and above the limb. A possible explanation for the redshift at the limb could be the following. Our observation was made in October, when the north pole of the solar rotation axis was tilting toward the Earth. If we simply assume that plasma is flowing outward along a super-radial expanding funnel structure at the north limb, then we will see redshift at the side away from the Earth and blueshift at the side toward the Earth. Our derived Doppler shifts will be changed if we assume that the limb emission is at rest. However, the trend of larger blueshift with increasing temperature should remain, since the redshift at the limb is larger at higher temperatures.

Del Zanna (2008) studied the temperature-dependent upflows at the boundary of an active region, which might be related to the origin of the slow solar wind (Harra et al. 2008). The blueshift at the boundary of the active region also increases with increasing temperature, and the values of the coronal Doppler shift in Del Zanna (2008) are close to those obtained in the coronal hole here. In a recent solar wind model presented by Cranmer et al. (2007), the outflow speeds for the fast and slow solar wind are about 30 km s^{-1} at the height of 0.2 solar radii, and are not so different below 0.2 solar radii above the photosphere. Because of the exponentially decreasing electron density above the photosphere, it is likely that most of the coronal emission recorded by EIS comes from a certain height range below 0.2 solar radii. Thus, the model results in Cranmer et al. (2007) seem to be consistent with EIS observations.

Flare and CME related outflows were also found by Imada et al. (2007) and Jin et al. (2009). However, these transient outflows seem to start in the lower TR (formation height of He II) and reach tens or even more than hundreds of km s^{-1} in the corona. Moreover, the trend of the upflow dependence on temperature dramatically changes at ~1 MK during flares and CMEs. While both of our Figure 3 and Figure 3 in Del Zanna (2008) seem to suggest a steady acceleration of the solar wind. Thus, behaviors of the solar wind at its origin and of the CME/flare during initiation are largely different.

The temperature variation of the difference of Doppler shift between the coronal hole and quiet Sun as shown in Figure 3(d) is also consistent with the SUMER result at $\lg(T/\mathrm{K}) \leqslant 6.0$ (Xia et al. 2004). The significant blueshift in the coronal hole with respect to the quiet Sun suggests that the solar wind outflow starts in the TR, and corresponding signatures are probably present at temperatures as low as $\lg(T/\mathrm{K}) = 5.4$. Our new result based on EIS observational data complements the earlier SUMER result, as we find that the difference of the Doppler shifts between the coronal hole and the quiet Sun increases with temperature from $\lg(T/\mathrm{K}) = 5.4$ to $\lg(T/\mathrm{K}) = 6.3$.

EIS is an instrument on board *Hinode*, a Japanese mission developed and launched by ISAS/JAXA, with NAOJ as domestic partner and NASA and STFC (UK) as international partners. It is operated by these agencies in cooperation with ESA and NSC (Norway). Hui Tian and Chuanyi Tu are supported by the National Natural Science Foundation of China under contracts 40874090 and 40931055.

REFERENCES

Aiouaz, T., Peter, H., & Lemaire, P. 2005, A&A, 435, 713
Antonucci, E. 2006, Space Sci. Rev., 124, 35
Banerjee, D., Pérez-Suárez, D., & Doyle, J. G. 2009, A&A, 501, L15
Bell, B., & Noci, G. 1976, J. Geophys. Res., 81, 4508
Brosius, J. W., Rabin, D. M., & Thomas, R. J. 2007, ApJ, 656, L41
Cranmer, S. R., van Ballegooijen, A. A., & Edgar, R. J. 2007, ApJS, 171, 520
Culhane, J. L., et al. 2007, Sol. Phys., 243, 19
Dammasch, I. E., Wilhelm, K., Curdt, W., & Hassler, D. M. 1999, A&A, 346, 285
Del Zanna, G. 2008, A&A, 481, L49
Dere, K. P., et al. 1997, A&AS, 125, 149
Gabriel, A. H., Bely-Dubau, F., & Lemaire, P. 2003, ApJ, 589, 623
Giordano, S., Antonucci, E., Noci, G., Romoli, M., & Kohl, J. L. 2000, ApJ, 531, L79
Gosling, J. T., et al. 1981, J. Geophys. Res., 86, 5438

Harra, L. K., et al. 2008, ApJ, 676, L147
Hassler, D. M., Dammasch, I. E., Lemaire, P., Brekke, P., Curdt, W., Mason, H. E., Vial, J.-C., & Wilhelm, K. 1999, Science, 283, 810
He, J.-S., Tu, C.-Y., & Marsch, E. 2007, A&A, 468, 307
He, J.-S., Tu, C.-Y., Tian, H., & Marsch, E. 2009, Adv. Space Res., in press
Imada, S., et al. 2007, PASJ, 59, S793
Jin, M., Ding, M. D., Chen, P. F., Fang, C., & Imada, S. 2009, ApJ, 702, 27
Kamio, S., et al. 2007, PASJ, 59, S757
Kohl, J. L., Noci, G., Cranmer, S. R., & Raymond, J. C. 2006, Astron. Astrophys. Rev., 13, 31
Kohl, J. L., et al. 1995, Sol. Phys., 162, 313
Kojima, M., et al. 1999, J. Geophys. Res., 104, 16993
Krieger, A. S., Timothy, A. F., & Roelof, E. C. 1973, Sol. Phys., 29, 505
Landi, E., et al. 2006, ApJS, 162, 261
Lemaire, P., et al. 1997, Sol. Phys., 170, 105
Mariska, J. T., et al. 2007, PASJ, 59, S713
Marsch, E., Tian, H., Sun, J., Curdt, W., & Wiegelmann, T. 2008, ApJ, 684, 1262
McComas, D. J., et al. 1998, Geophys. Res. Lett., 25, 1
McIntosh, S. W., et al. 2007, ApJ, 654, 650
Milligan, R. O., & Dennis, B. R. 2009, ApJ, 699, 968
Noci, G., & Gavryuseva, E. 2007, ApJ, 658, L63
Peter, H., & Judge, P. G. 1999, ApJ, 522, 1148
Sakao, T., et al. 2007, Science, 318, 1585
Schrijver, C. J. 2001, ApJ, 547, 475
Telloni, D., Antonucci, E., & Dodero, M. A. 2007, A&A, 472, 299
Teriaca, L., Poletto, G., Romoli, M., & Biesecker, D. A. 2003, ApJ, 588, 566
Tian, H., Curdt, W., Marsch, E., & He, J.-S. 2008d, ApJ, 681, L121
Tian, H., Marsch, E., Curdt, W., & He, J.-S. 2009, ApJ, 704, 883
Tian, H., Marsch, E., Tu, C.-Y., Xia, L.-D., & He, J.-S. 2008a, A&A, 482, 267
Tian, H., Tu, C.-Y., Marsch, E., He, J.-S., & Zhou, G.-Q. 2008b, A&A, 478, 915
Tian, H., Xia, L.-D., He, J.-S., Tan, B., & Yao, S. 2008c, Chin. J. Astron. Astrophys., 8, 732
Tu, C.-Y., Zhou, C., Marsch, E., Xia, L.-D., Zhao, L., Wang, J.-X., & Wilhelm, K. 2005, Science, 308, 519
Wang, Y.-M., Sheeley, N. R., Jr., & Nash, A. G. 1990, Nature, 347, 439
Wilhelm, K., et al. 1995, Sol. Phys., 162, 189
Wilhelm, K., Dammasch, I. E., Marsch, E., & Hassler, D. M. 2000, A&A, 353, 749
Xia, L.-D., Marsch, E., & Curdt, W. 2003, A&A, 399, L5
Xia, L.-D., Marsch, E., & Wilhelm, K. 2004, A&A, 424, 1025
Young, P. R., et al. 2007, PASJ, 59, S857